



Title	On limit strength of frozen clay undergoing triaxial tension
Author(s)	Nishimura, Satoshi; Kawasaki, Hidetoshi; Sato, Issei
Citation	Géotechnique, 1-13 https://doi.org/10.1680/jgeot.22.00192
Issue Date	2023-01-19
Doc URL	http://hdl.handle.net/2115/91068
Type	article (author version)
File Information	manuscript_HUSCAP.pdf



[Instructions for use](#)

ON LIMIT STRENGTH OF FROZEN CLAY UNDERGOING TRIAXIAL TENSION

Satoshi Nishimura^{1,*}, Hidetoshi Kawasaki² and Issei Sato³

¹Faculty of Engineering, Hokkaido University, Japan (*Corresponding author)

²Formerly School of Engineering, Hokkaido University, Japan

³Kajima Technical Research Institute, Kajima Corporation, Japan

ABSTRACT

A new interpretation of failure of frozen clay in tension is presented, through a unique test program applying 'triaxial tension', in which the axial stress was reduced to negative values while zero or positive radial stress was maintained. The limit strength is determined by a meeting point of two competing mechanisms – strain-hardening in shear, and progressively degrading tensile strength as the shear deformation disturbs the soil structure. In some conditions, the limit strength observed in tension is actually given by the shear resistance limit, not by a true tensile strength. This interpretation is successful in explaining apparently unclear confining stress-dependency of the observed failure envelopes at low stresses. The influence of the pre-freezing effective stress, post-freezing total stress and pre-freezing pore water pressure on the strength was also investigated. The tensile strength degradation was formulated by using the specific work input to estimate the operational tensile strength and the strain at which a tensile rupture occurs. Cooling after shear deformation apparently healed the damage and recovered the initial tensile strength, allowing the stress-strain curve to significantly overshoot the proposed tensile strength line. Explaining the combined influence of shear and temperature history on the tensile strength – work relationships requires further study.

INTRODUCTION

Recent underground projects involve complex excavation processes at greater depths reaching 40-50 m more commonly than ever, often adjacent to existing substructures and/or under soft and unstable ground conditions. Some processes, such as tunnel connection and enlargement, require prior stabilisation of surrounding ground. Artificial Ground Freezing (AGF) is an effective technique to stabilise selected localities with high accuracy and reliability. As the recent innovation allows freezing at lower temperatures (for example, circulation of CO₂, in lieu of conventional brine, can cool the chiller pipes down to -45 °C; Tsuji and Yoshida, 2019), frozen domains are expected to mobilise higher strength. Even colder liquid nitrogen (LN) has long been available for smaller-scale, short-term work, but it is usually produced in remote factory plants, and the freezing was typically one-off and expensive. The above development opens up more possibilities in design, for example by using thinner frozen soil as load-bearing roofs or earth-retaining walls. While keeping the frozen

soil thinner is highly cost-effective due to significant reduction in the required heat-conduction time, it risks subjecting the soil to bending in some parts. In this scenario, the design based only on the compressive or shear strength of frozen soil is inappropriate, as the tensile strength limits the bending resistance of the frozen soil. These facts point to importance of an appropriate testing method to characterise the tensile failure in frozen soils, and mechanical theory and insights to interpret the results.

In the context of deep underground application, it is important to note that considerable total and effective stresses, as well as large pore pressure, exist at the time of freezing, and that they may partially remain even during the excavation processes. As will be reviewed, conventional tension tests on frozen soils have been almost all performed in unconfined states, mostly with soil samples frozen unconfined too. This conventional approach severely limits the possibility of interpreting the frozen soil's failure behaviour in tension by drawing a parallel to the effective-stress-based unfrozen soil mechanics, as will be discussed in the next section. A particularly relevant example of deep AGF application is Trans-Tokyo Bay (Aqua-Line) Expressway in Japan (e.g. Uchida et al., 1993). This project involved construction of submarine tunnels passing through soft alluvial clay at some 40-55 m below the sea level (20-35 m below the sea bottom) and vertical shafts connected to them, assisted partially by AGF (e.g. Akagawa, 2021). The pore pressure at the invert level was about 600 kPa. A high pore (back) pressure usually prevents tensile failure in unfrozen soft clays by preventing cavitation. It is not clear, however, how this condition affects the tensile failure of frozen clay, nor is it possible to address this issue by the conventional testing methods with no control of confining stress and pore pressure. AGF case histories under similarly deep settings with high water pressure or soft soil conditions have also been reported elsewhere (e.g. Ou et al., 2009; Viggiani et al., 2015).

This study adopted a new laboratory test approach by developing 'triaxial tension' testing, in which tensile loading was undertaken with lateral confinement. In contrast to conventional triaxial extension, it allows the minor (total) principal stress σ_3 to go negative (i.e. active pulling). Freezing was performed directly after consolidation while the specimen remained under confinement, by improving the method by Wang et al. (2017). To the authors' knowledge, no similar attempt has been reported so far. This study, after considerable trial and error, eventually found a set-up allowing stable temperature control and providing repeatable results.

This paper will firstly review the basic mechanics of unfrozen soils under tensile loading, which may involve either shear failure or tensile failure. A review of previous studies on tensile strength of frozen soils will be then given to underline the need for this study's approach. In the authors' view, investigation on the tensile failure of frozen soils must answer the following questions:

(i) Is the limit strength of frozen soils in tension determined by a 'tensile strength' (i.e. σ_3 limit),

independently from shear strength (deviator stress q limit)?

(ii) Is the tensile strength affected by the initial, pre-freezing pore pressure and the effective stress?

(iii) Is the peak tensile limit, whatever (i) reveals, to be relied upon in design, given the eventually inevitable strain-softening and fracturing?

(iv) How are all the above affected by conditions such as water content w (intertwined with the above issue of the consolidation effective stress), temperature and strain rate?

The present study provides new, if not comprehensive, insights to these questions through a systematic series of high-quality, repeatable triaxial tension tests in which the pre- and post-freezing stress and the initial pore water pressure were systematically varied. Additional tests adopted complex loading histories involving temperature changes, lateral stress changes and a loading pause.

This study only considers saturated clay, as initial phase of more thorough investigation. This paper uses 'extension' to mean geometric elongation, and 'tension' to mean imposition of an absolute negative normal stress.

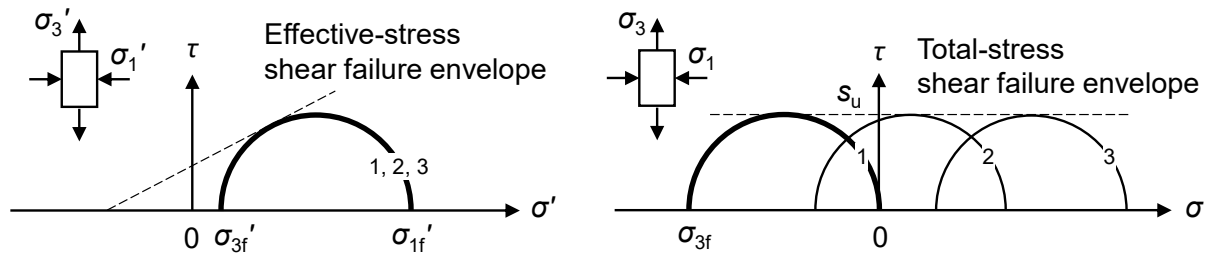
TENSILE STRENGTH OF UNFROZEN AND FROZEN SATURATED SOILS: A REVIEW

Basic mechanics of (unfrozen) saturated soils under tensile loading

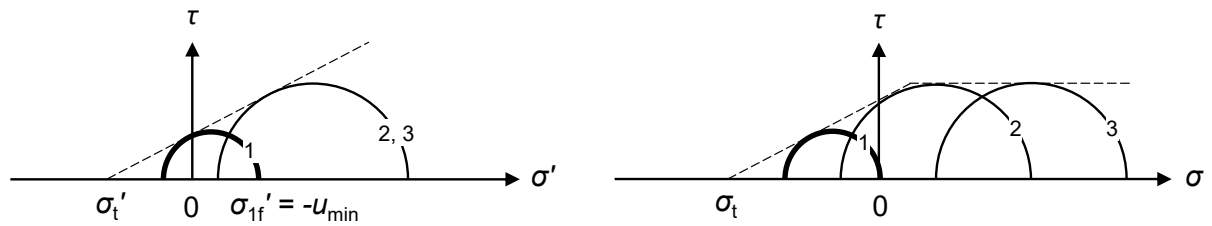
It may be helpful to briefly review elementary unfrozen soil mechanics concerning tensile failure. The discussion shall be limited to saturated soil in undrained triaxial conditions. In the simplest case (**Figure 1(a)**), when the initial pore water pressure (or the back pressure) u_0 has ample room for reduction, any total stress change, including the average confining total stress decrease due to tensile loading, is compensated by a negative excess pore water pressure under undrained conditions. As a result, the eventual effective stress is unaffected by the total stress changes, and thus the failure occurs when the deviator stress q reaches $2s_u$, where s_u is the undrained shear strength. The pattern is basically a shear failure in triaxial extension, even when the soil is undergoing tension in total stress term (i.e. negative σ_3).

The second pattern, illustrated in **Figure 1(b)**, occurs when the pore pressure u decreases to a limit value u_{\min} , and ceases to compensate the total stress changes for any more σ_3 reduction. In coarse-grained soils, this may correspond to cavitation pressure of the pore fluid. For finer-grained soils, u_{\min} may be smaller than the vacuum and sustain high suction. If the pore pressure remains at u_{\min} for further tensile loading, the total stress reduction is directly reflected on the effective stress, and when the latter reaches the failure envelope, failure will occur. It is more likely in reality that, when the pore pressure reaches u_{\min} , the system cannot maintain undrained conditions, and u_{\min} rebounds to the atmospheric pressure, causing abrupt tensile failure. For this scenario, the total stress application under undrained conditions before tensile loading influences the eventual tensile strength by raising u , and allowing σ_3 to decrease more before u decreases to u_{\min} .

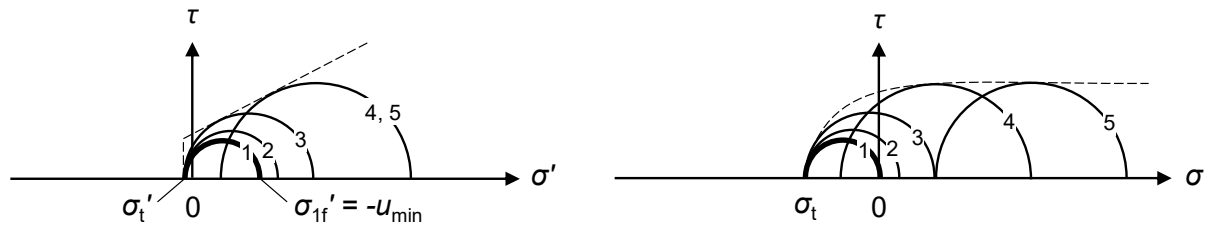
In fact, there is no a priori reason to assume that the effective-stress failure envelope is linear. The true tensile strength σ'_t on the effective stress σ' -axis may not be where extrapolation of the shear failure line would suggest. The third pattern, illustrated in **Figure 1(c)**, is a likely response in this case. When the failure is caused by u meeting u_{\min} , and σ' meeting σ'_t , this is considered to be a pure tensile failure, with σ_3 at failure unaffected by initial confining stress (Mohr's stress circles 1-3 in **Figure 1(c)** right).



(a) Case of sufficient back pressure u_0 relative to s_u : Shear failure



(b) Case of small back pressure u_0 relative to s_u : Shear failure with pore cavitation



(c) Case of small back pressure u_0 relative to s_u and tension cutoff: Tensile failure with pore cavitation

Figure 1: Failure scenarios in triaxial tension in unfrozen saturated soils
(subscript f denotes failure state)

These scenarios are relatively simple to discern when the pore water pressure is measured in unfrozen soil. In frozen soil, however, measuring liquid and ice water pressures accurately is not

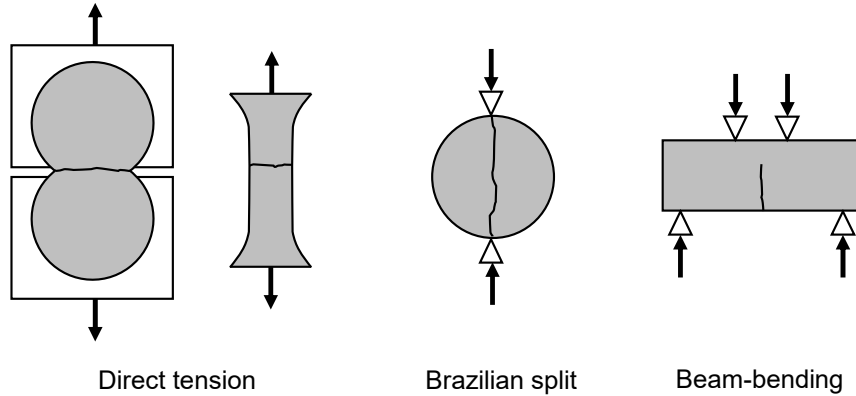
an established technique, and no direct manner of observation is possible. The idea in this study is therefore to observe how the σ_3 limit in tensile loading varies with the major principal stress σ_1 . If σ_3 at failure, σ_{3f} , shifts in parallel with σ_1 , what is perceived as ‘tensile strength’ in frozen soil may in reality be governed by the shear strength. If σ_{3f} is unaffected by σ_1 , on the contrary, the pore materials (ice and liquid) and the soil skeleton may be truly being pulled apart on the perpendicular plane. This logic must also be checked with visual observation of the failed specimen.

Testing methods for tensile strength

The tensile strength of frozen soils has been conventionally investigated by three testing methods; direct tension, Brazilian splitting and beam-bending, as illustrated in **Figure 2**. Haynes and Karalius (1977), Eckardt (1982) and Zhu and Carbee (1985; 1987), among others, adopted cylindrical specimens with enlarged ends in direct tension. Eckardt (1982) penetrated nails to the specimen ends to ensure the soil-machine coupling. Zhang et al. (2019) tested regular cylindrical specimens, attached to loading plates with epoxy adhesive. In the other studies, the coupling mechanisms are not clearly explained. Akagawa and Nishisato (2009) and Li et al. (2018) adopted ‘8-shaped’ specimens (the leftmost in **Figure 2**), following Tamrakar et al. (2007). All these studies performed tension tests in unconfined states. One possible exception is a study by ‘Jessberger/Ebel’ mentioned in Jessberger’s (1981) state-of-the-art paper, of which drawing suggests application of radial pressure. However, the source is not cited, and more detail could not be found. Apart from this, there has been no systematic study conducting ‘triaxial tension’ testing, to the authors’ knowledge.

Brazilian split (Bragg and Andersland, 1982; Zhou et al., 2015; You et al., 2021) and beam-bending (Azmatch et al., 2011; Yamamoto and Springman, 2017) tests have also been performed to obtain the tensile strength or observe fracture processes of frozen soils. While these tests are relatively straightforward in principle, the stress field is non-uniform within the specimen. Namikawa and Koseki (2007) compared the above two testing methods with direct tension for cement-treated sand both experimentally and numerically, and concluded that the direct tension test gives the most accurate tensile strength, while the other two are affected by local shear and progressive failure. It would be also difficult to apply confining stress in these two testing methods.

The literature review suggests that there has been no experimental data or attempt of applying tension from confined states, which, as discussed earlier, would clarify at what conditions the frozen soil fails in shear or reaches a true tensile limit. This background led to development of triaxial tension testing in this study.



Direct tension Brazilian split Beam-bending

Figure 2: Conventional tensile strength tests for soils

MATERIAL AND TESTING METHOD

Apparatus

Triaxial apparatus was modified to allow direct tension testing of frozen soils under confining pressure. The system is illustrated in **Figure 3**. The whole system was installed and operated in a room at a temperature of 25 °C. A unique feature of this apparatus is that it allows freezing a soil specimen within the cell, unlike in many other studies in which samples pre-frozen in a separate freezer were transferred to testing machines. This feature permits freezing without releasing the stress after consolidation in unfrozen states, as it happens in-situ. This freezing method prevents unnatural cracking and inhomogenisation due to unconfined freezing (Wang et al., 2017). The freezing is performed by firstly draining out the confining water slowly via an adjustable valve lest the cell pressure drops, and then by pumping in pre-cooled refrigerant into the cell, again slowly not to change the cell pressure. The cooling mechanism was modified from the earlier study by Wang et al. (2017). The refrigerant is controlled via two lines. Line 1 is connected to a pressurised tank in the cold bath, from which the pre-cooled refrigerant (ethylene glycol) is sent to the pressurised triaxial cell. This line was used to adjust the refrigerant level in the triaxial cell. Line 2 circulates the refrigerant through the heat exchange coil. This line was used to maintain and adjust the temperature in the triaxial cell. The temperature control of the refrigerant directly in contact with the specimen by Line 2 is much more responsive than more indirect manners, such as controlling the room ambient temperature or placing a heat exchanger within the cell. All through these operations, the cell pressure could be controlled independently (kept constant in this study).

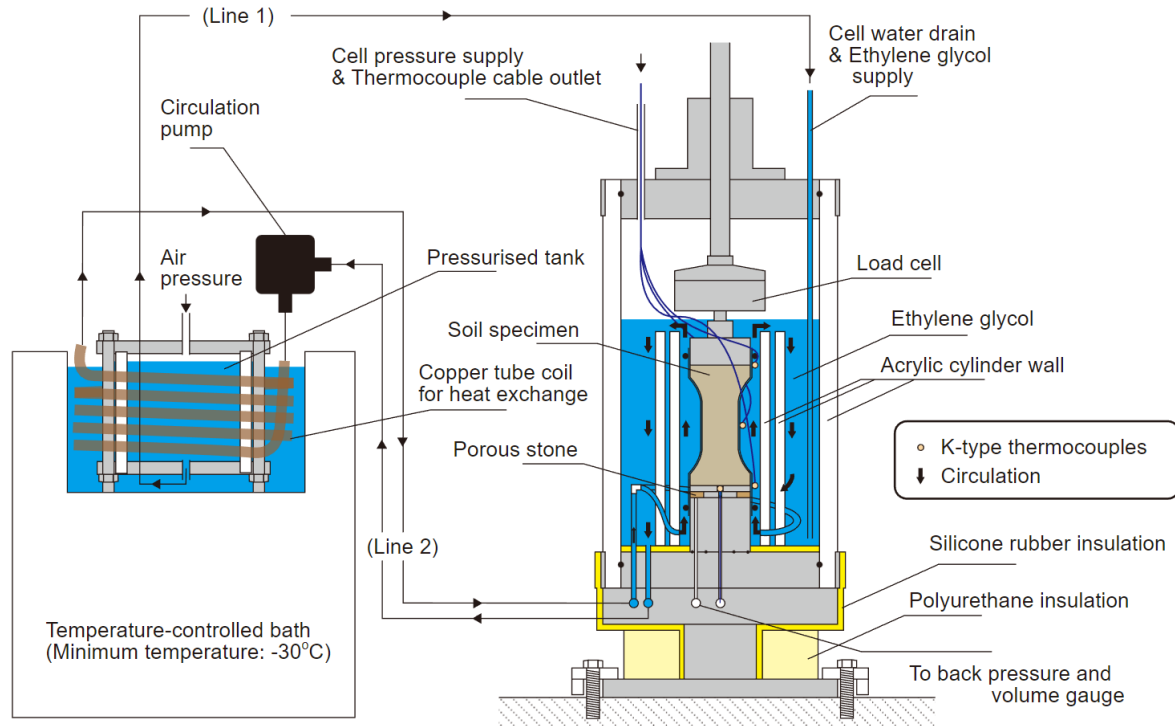
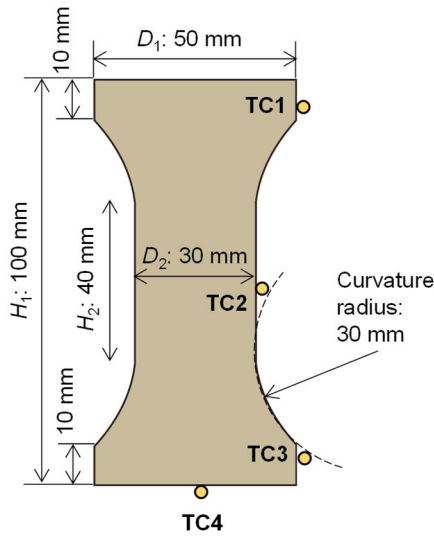


Figure 3: Triaxial tension test apparatus for frozen soil

Higher cooling efficiency was achieved by setting a double acrylic wall around the specimen and restricting the circulation path. This cell-in-a-cell proved very effective in insulating the specimen from the room environment. The refrigerant comes to contact with the specimen first as it enters the triaxial cell, and thus effectively deprives the heat from the specimen before receiving heat from outside. For $-30\text{ }^{\circ}\text{C}$ set at the cold bath, $-23\text{ }^{\circ}\text{C}$ was achieved at the specimen surface. This is much higher cooling efficiency than in the previous design (Wang et al., 2017). The refrigerant outside the inner double-wall works as a buffer, and was only mildly cold. This helps limiting the outer cell surface frosting that hinders visual inspection. Another improvement was to use a taller pedestal. The specimen bottom was slightly warmer in this apparatus due to the heat leak through the pedestal. A taller pedestal alleviated this problem. The temperature was measured by K-type thermocouples at four locations, three at the specimen's outer surface and one at the bottom end centre (**Figure 4**). TC1 was at $-14\sim-13\text{ }^{\circ}\text{C}$ when TC2-TC4 were at $-15\text{ }^{\circ}\text{C}$. This difference was smaller for higher temperatures.

The axial ram was driven by a very precise and powerful direct-drive motor capable of applying compression and extension loads equally. Pore water drainage during consolidation was allowed towards the porous stone ring (**Figure 3**) embedded in the pedestal via filter paper strips attached to the specimen's lateral surface (**Figure 4** right).



(a) Dimensions and thermocouples (TC)

(b) Specimen, as trimmed, and as enclosed by rubber membrane with filter paper strips

Figure 4: Specimen geometry and dimensions

The soil specimens were trimmed into a dumbbell shape with enlarged ends, as illustrated in **Figure 4**. The diameters of the middle part and the enlarged ends were 30 mm and 50 mm, respectively. The total height was 100 mm. The ends were trimmed smoothly, and simply put into contact with smooth metal platen surfaces. The soil-platen coupling to transmit a tensile load was established solely by freezing adhesion. It was therefore unnecessary to perform any special treatment during specimen set-up in this study. The bottom platen was polished stainless steel, and the top platen was anodised aluminum. The cross-sectional area ratio between the specimen ends and middle is 2.8. The tensile failure is therefore forced to occur in the middle part as long as the platen-specimen adhesion is greater than $1/2.8$ of the tensile strength. The transition from the middle to the enlarged parts had a gentle curvature with a radius of 30 mm to avoid stress concentration. This geometry was successful in causing the failure in the middle part. By adopting the quick freezing under confining pressure, the water content ratio of the middle part to the ends, as measured after freezing, was 0.996-0.1011, meaning almost no internal axial water migration. Wang et al. (2017) observed slightly greater radial water migration, with a rim-to-core water content ratio of 1.03 on average for 30 mm-diameter Kasaoka clay specimens. This is still small and accepted in this study.

Material and specimens

Reconstituted saturated samples of Kasaoka clay were tested in this study. The clay has been extensively tested in frozen states by the first author in the past. The physical properties are shown

in **Table 1**. The gravimetric unfrozen water contents w_u measured at several temperatures by Nuclear Magnetic Resonance (NMR) are shown in **Figure 5**, along with the calculated degree of liquid saturation S_l . The clay was made into slurry at the water content $w=100\%$, then mixed and poured into a 220mm-diameter consolidometer under vacuum for de-airing, and then one-dimensionally pre-consolidated. Thus prepared samples were saturated, showing B value > 0.95 . Nine specimens were taken from each consolidated cake. The sample pre-consolidated at $\sigma_{vp}'=100$ and 200 kPa were used for tests with pre-freezing isotropic effective stress $p_c'=100$ and 600 kPa, respectively. Ideally, σ_{vp}' should have been smaller than 50 kPa for $p_c'=100$ kPa so that the effect of one-dimensional consolidation would be eventually erased at p_c' . However, such a soft specimen was difficult to be prepared into the desired shape. The specimens were formed by carefully trimming along curved guides in a rotary soil lathe.

Wang et al. (2017) and Nishimura and Wang (2019) presented the triaxial compression strength of Kasaoka clay prepared in a similar manner. At -10, -5 and -2 °C, the clay did not exhibit any change of strength against post-freezing total stress p_f in the range of 200-600 kPa, as shown in **Figure 6** (solid markers; note that the ultimate strength, not the peak strength, was published by Nishimura and Wang, 2019), unlike against the pre-freezing stress (open markers). This insensitivity to p_f is a characteristic of fine-grained soils, seen in other earlier studies too (e.g. Chamberlain et al., 1972; Wang et al., 2004). Inspired by Ladanyi and Morel (1990), Nishimura and Wang (2019) explained this by less dilative nature of fine-grained soils leading to shear failure in the pattern of **Figure 1(a)** right. Although there has been clear evidence that polycrystalline ice's strength is pressure-dependent (Rist and Murrell, 1994; Singh and Jordaan, 1996; Shulson, 2001), the ice in smaller pores in fine-grained soils may have less micro-defects that respond to confining pressure.

Table 1: Physical properties of Kasaoka clay

Plastic limit (%)	Liquid limit (%)	Particle density (Mg/m ³)	Percentage finer than 2/5/63/75 μm (%)
28	62	2.65	40/60/98/100

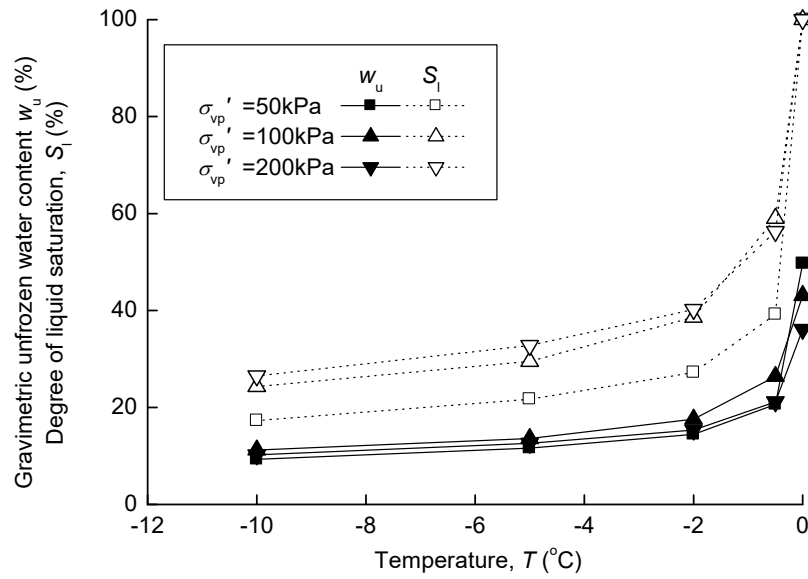


Figure 5: Gravimetric unfrozen water content w_u and degree of liquid saturation S_l in frozen Kasaoka clay one-dimensionally consolidated at σ_{vp}'

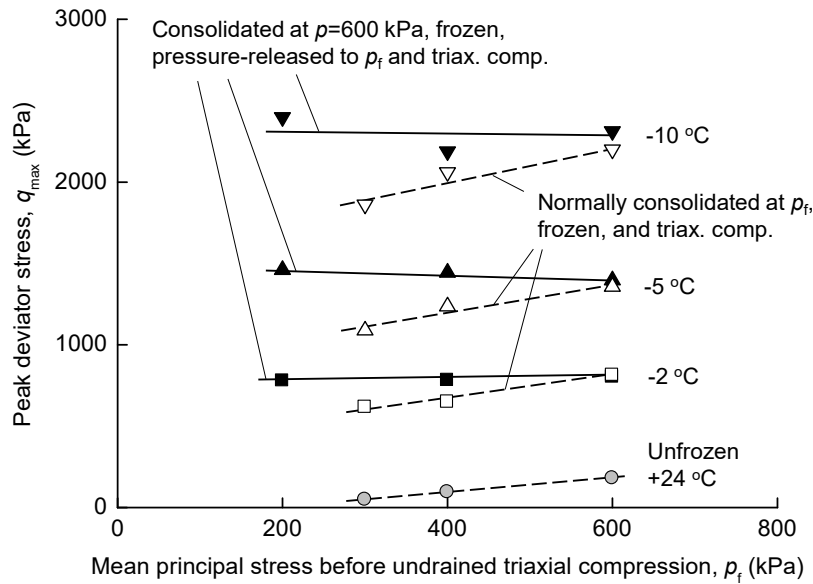


Figure 6: Triaxial compression peak strength of frozen Kasaoka clay: Influence of pre- and post-freezing stress changes (pre-freezing back pressure=200 kPa in all cases)

Test program

30 triaxial tension tests were performed in total, as summarised in **Table 2**. The main variables were the temperature T (-1, -4, -9 or -15 °C), pre-freezing effective consolidation stress p_c' (100 or 600 kPa) and post-freezing total stress p_f (0, 200 or 650 kPa). A series consisting of Tests 1-23 covers all the combinations of these, except $p_f=0$ kPa at -1 °C. The adhesion at the bottom end

turned out to be too weak in this condition to apply tension. Note that the T values cited are nominal, and the measured values are shown in **Table 2**. They are taken from thermocouple TC2, since the failure occurred in the specimen middle.

Table 2: List of performed triaxial tension tests

ID	T (°C)		p_c (kPa)	p_c' (kPa)	u_c (kPa)	p_f (kPa)	$e_c^{(2)}$	Note
	Nominal	Measured ¹⁾						
1		-0.71	200	100	100	200	1.133	
2		-0.63	200	100	100	650	1.129	
3	-1	-0.78	650	600	50	200	0.819	
4		-0.75	650	600	50	650	0.802	
5		-0.63	650	600	50	200	0.802	(Duplicate of Test 3)
6		-4.2	200	100	100	0	1.123	
7		-4.0	200	100	100	200	1.131	
8	-4	-4.4	200	100	100	650	1.126	
9		-4.3	650	600	50	0	0.796	
10		-4.4	650	600	50	200	0.797	
11		-4.3	650	600	50	650	-. ³⁾	
12		-8.3	200	100	100	0	1.109	(Slightly warm)
13		-9.0	200	100	100	200	1.129	
14	-9	-9.2	200	100	100	650	1.114	
15		-8.9	650	600	50	0	0.798	
16		-9.2	650	600	50	200	0.801	
17		-9.0	650	600	50	650	-. ³⁾	
18		-14.4	200	100	100	0	1.104	
19		-14.7	200	100	100	200	1.099	
20	-15	-14.5	200	100	100	650	1.105	
21		-14.6	650	600	50	0	0.794	
22		-14.6	650	600	50	200	0.798	
23		-14.6	650	600	50	650	0.795	
24		-14.7	650	100	550	0	1.116	
25	-15	-14.7	650	100	550	200	1.102	
26		-14.7	650	100	550	650	1.112	
27	-4 to -15	-4.2 to -14.7	650	600	50	650	0.792	Pause and T change
28	-4	-4.3	650	600	50	650	-. ³⁾	Pause
29	-15	-14.7	650	600	50	650	0.799	Pause
30	-4	-4.4	650	600	50	σ_1 : 650 to 0	0.791	σ_1 change

¹⁾ Mid-height thermocouple (TC2), average over 2,000 sec around the tensile peak

²⁾ e_c : Void ratio after consolidation

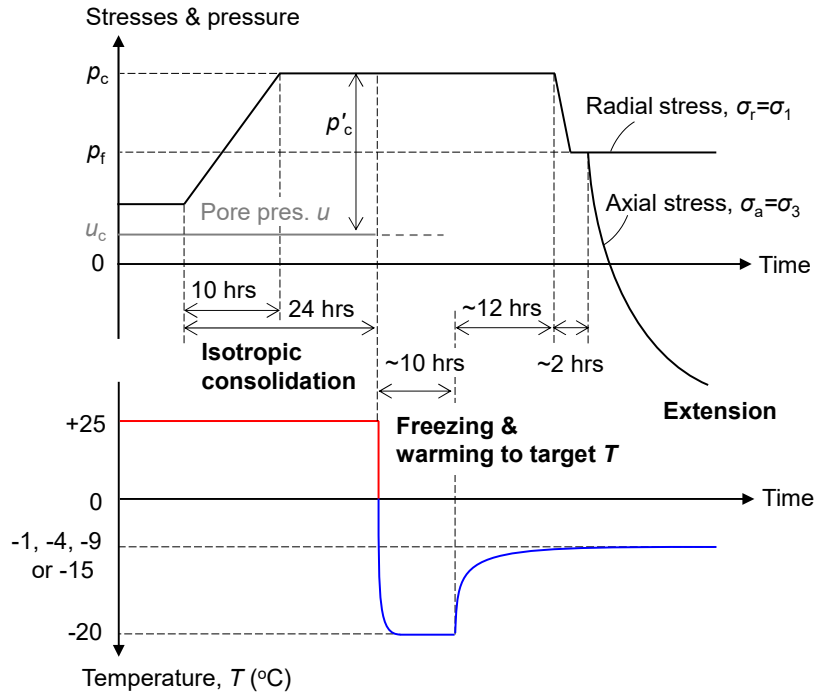
³⁾ Final water content could not be measured accurately due to membrane rupture when removing the specimen

The back pressure after consolidation u_c was basically 100 kPa for $p_c'=100$ kPa, and 50 kPa for $p_c'=600$ kPa. Ideally, the latter would have been set at 100 kPa too – however, the slightly smaller value had to be accepted due to the cell capacity of 700 kPa. In Tests 24-26, $u_c=550$ kPa was set

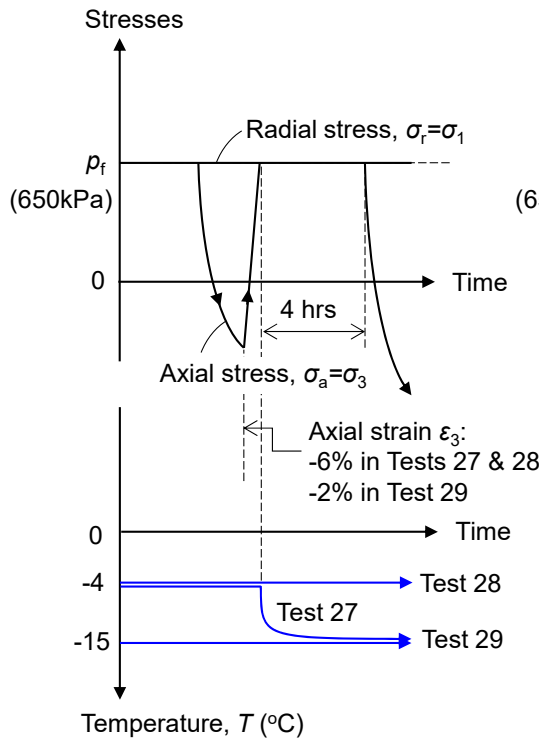
for $p_c'=100$ kPa. Test 5 is a duplicate test of Test 3 performed early in the program, out of a concern about test repeatability, as a slight temperature fluctuation has relatively large influence on the result at such high temperatures as -1 °C. Tests 18-26 constitute an interesting comparative set, allowing observation of influence of p_c' , p_r and u_c independently while keeping the other two constant ($u_c=50$ kPa and 100 kPa are assumed nearly equal here).

The above basic series (Tests 1-26) were conducted in the following steps. Firstly, the pre-consolidated, unfrozen specimen was set up in the apparatus after being covered with a rubber membrane with a diameter of 30 mm. The enlarged part therefore underwent greater membrane force, as the membrane size was chosen for the middle part. This influence was not deemed important, as the failure always occurred at the specimen middle. After being isotropically consolidated to p_c' , the specimen was frozen under constant cell pressure, as described earlier. This process was undrained. The convergence of axial displacement can be considered to mark temperature equilibrium, and the freezing was complete in 20 minutes. At this moment, the specimen was frozen at -20 °C, and this state was kept at least for 10 hours. The temperature was then increased to a target value. The change was fully transferred to the specimen core within an hour (as inferred from TC4 and numerical analysis), but about 12 hours were allowed for ensuring equilibration. The total stress was then changed to p_r in an hour, and after the axial strain rate became smaller than 10^{-4} %/min, the extension stage was initiated. These stages are illustrated in **Figure 7(a)**.

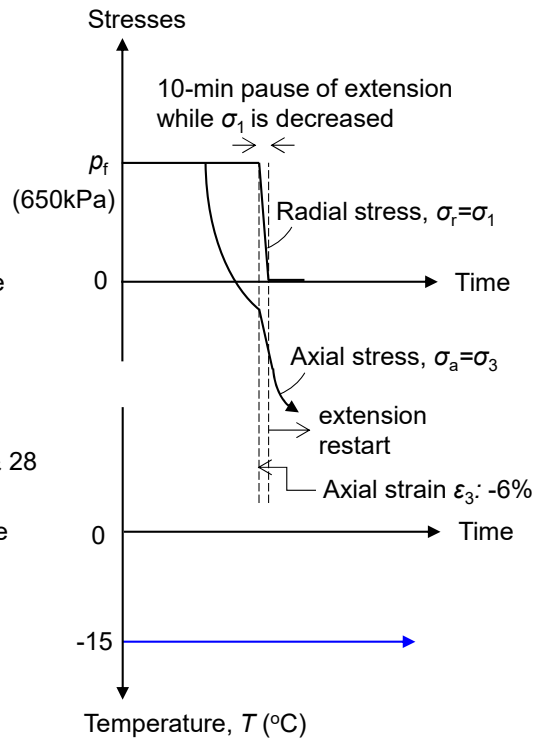
The extension was applied at a constant axial strain rate of -0.05 %/min. This rate was sufficiently slow for the frozen clay to remain well in the static, ductile regime (e.g. Parameswaran 1980) but allows a failure to be reached within the day under the operator's constant watch. In this paper, the nominal axial strain ϵ_a (=minor principal strain ϵ_3) is defined by the axial displacement d divided by the total specimen height H_1 (see **Figure 4**). Given the enlarged ends, this definition may underestimate the true strain in the middle, and is only nominal. The axial stress σ_a ($=\sigma_3$) is defined by the axial load divided by the mid-height cross-sectional area A_2 ($=\pi D_2^2/4$) after consolidation, without update for horizontal thinning due to extension. The deviator stress, q , is defined as the axial stress minus the radial stress (i.e. negative in axial tension).



(a) Tests 1-26: Constant T and σ_1 in extension stage



(b) Tests 27-29: 4-hour pause with or without T change



(c) Test 30: Decrease of σ_1 in extension stage

Figure 7: Variable control schemes in triaxial tension tests
(Pre-extension stages in (b) and (c) are same as (a))

Tests 27-30 were designed to investigate the influence of more complex state history on the failure. They followed the same steps except in the extension stage. Tests 27-29 involved unloading and reloading of deviator stress, with a 4-hour pause in between with or without temperature decrease, as illustrated in **Figure 6(b)**. The purpose of the pause was to allow temperature equilibration in Test 27, and to have the same time to failure as this in Tests 28 and 29. The intension will be discussed more later. The unloading in these tests started at $\epsilon_a=-6\%$ in Tests 27 and 28 ($T=-4\text{ }^{\circ}\text{C}$) and $\epsilon_a=-2\%$ in Test 29 ($T=-15\text{ }^{\circ}\text{C}$), approximately 75% of the tensile rupture strain observed in Tests 11 and 23, respectively. In Test 30, extension was paused at $\epsilon_a=-6\%$, the radial stress σ_1 was reduced from 650 to 0 kPa in 10 minutes, then the extension was resumed. This is illustrated in **Figure 6(c)**.

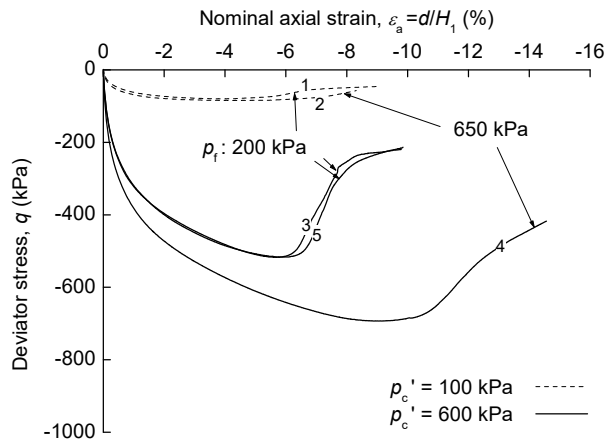
PEAK STRENGTH OBSERVED IN EXTENSION

Stress-strain relationships and failure patterns

The observed relationships between the deviator stress q and the nominal axial strain ϵ_a from Tests 1-23 are shown in **Figure 8** for different temperatures T . Consistency of Tests 3 and 5 assures the repeatability, even in sensitive temperature ranges. For $T=-4, -9$ and $-15\text{ }^{\circ}\text{C}$, the pre-peak parts of the curves are unique to each p_c' , unaffected by the post-freezing stress p_f . This is consistent with the earlier results in **Figure 6** showing no influence of the post-freeze stress change on the triaxial compression strength at moderate stress levels. Beyond the initial part, the influence of p_f becomes clearer, as the initially same stress-strain relationships start branching out one after another, starting from lower p_f , due to failure. In some cases ($T=-4$ and $-15\text{ }^{\circ}\text{C}$, $p_c'=100\text{ kPa}$), this occurred after common q peaks (-950 kPa and -2950 kPa, respectively) were reached, meaning that the minimum q value is unaffected by p_f , and only the post-failure strength reduction behaviour is different. For the rest of conditions, lower p_f led to slightly lower strength (i.e. higher q) as the stress-strain curves fell short of travelling up to the common q peak.

The peak strength (minimum q) is shown as Mohr's stress circles in **Figure 9**, along with earlier triaxial compression data obtained by the authors' team where the conditions are same (the difference in the strain rate, 0.01 %/min vs 0.05 %/min, is corrected by the observed rate-dependency; Wang et al., 2017). The failure envelopes are ambiguous when viewed with **Figure 1(a)-(c)** right as possible templates. As discussed above, some cases showed no influence of p_f on the strength, leading to a flat envelope in line with **Figure 1(a)** right. The others show only gentle slopes – far gentler than expected from the effective stress-based shear resistance angle ϕ' . Testing with negative σ_1 would lead to a clearer picture, but this all-round negative stress is an unlikely regime in field, and hard to achieve in tests too. Whilst it is probably reasonable to approximate ϕ as 0, except at $T=-1\text{ }^{\circ}\text{C}$, from **Figure 8** in practice, this 'as-plotted' Mohr's stress circle leaves ambiguity.

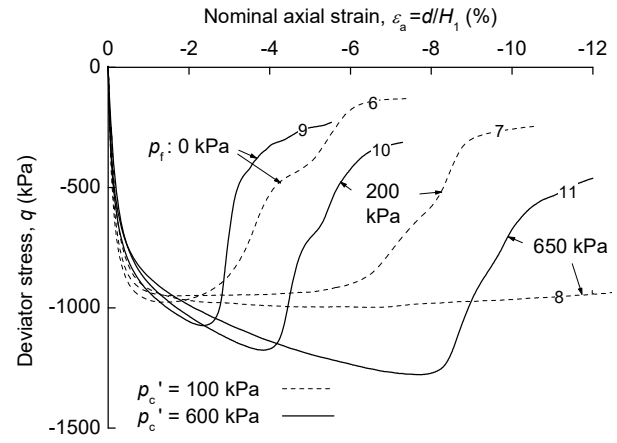
383



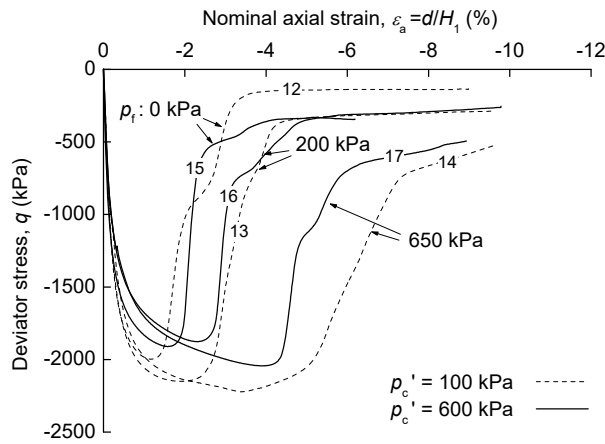
384

385

(a) $T = -1\text{ }^{\circ}\text{C}$



(b) $T = -4\text{ }^{\circ}\text{C}$

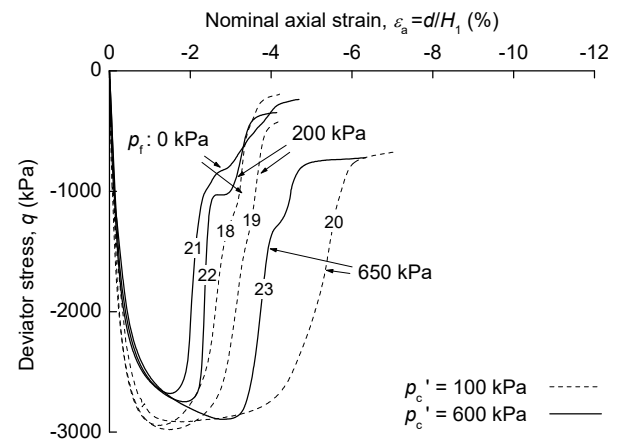


386

387

388

(c) $T = -9\text{ }^{\circ}\text{C}$



(d) $T = -15\text{ }^{\circ}\text{C}$

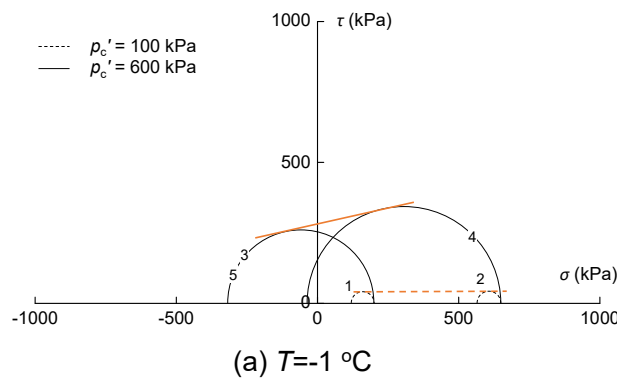
Figure 8: Deviator stress – axial strain relationships from Tests 1-23
(The numbers indicate test ID)

389

390

391

392



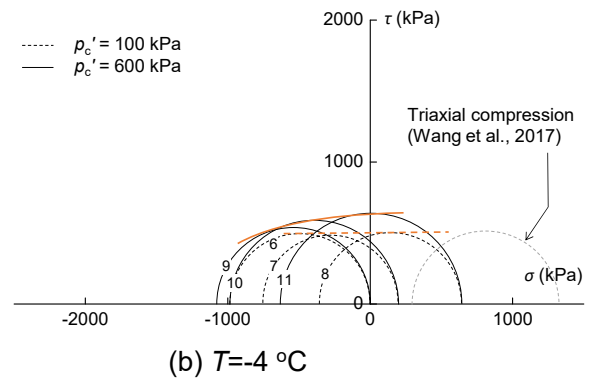
393

394

395

396

(a) $T = -1\text{ }^{\circ}\text{C}$



(b) $T = -4\text{ }^{\circ}\text{C}$

(Figure 9: Continues to next page)

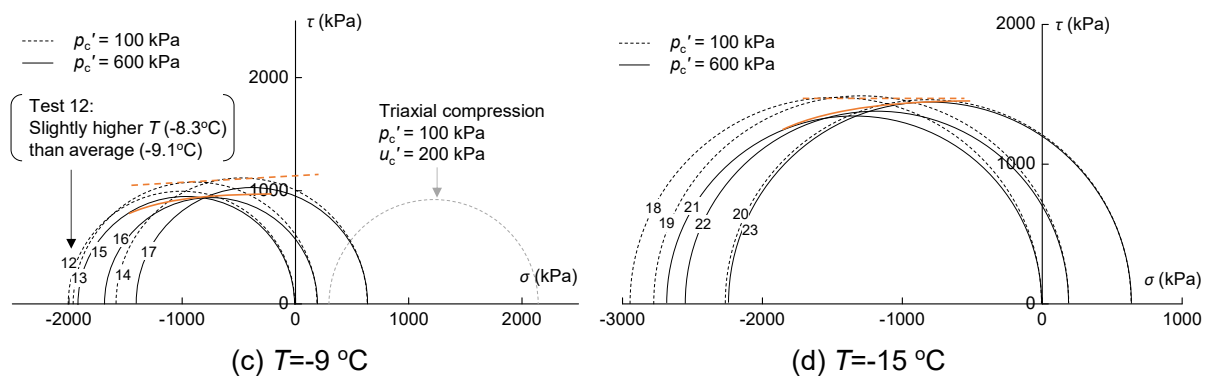


Figure 9: Mohr's stress circles for peak deviator stress from Tests 1-23
(The numbers indicate test ID)

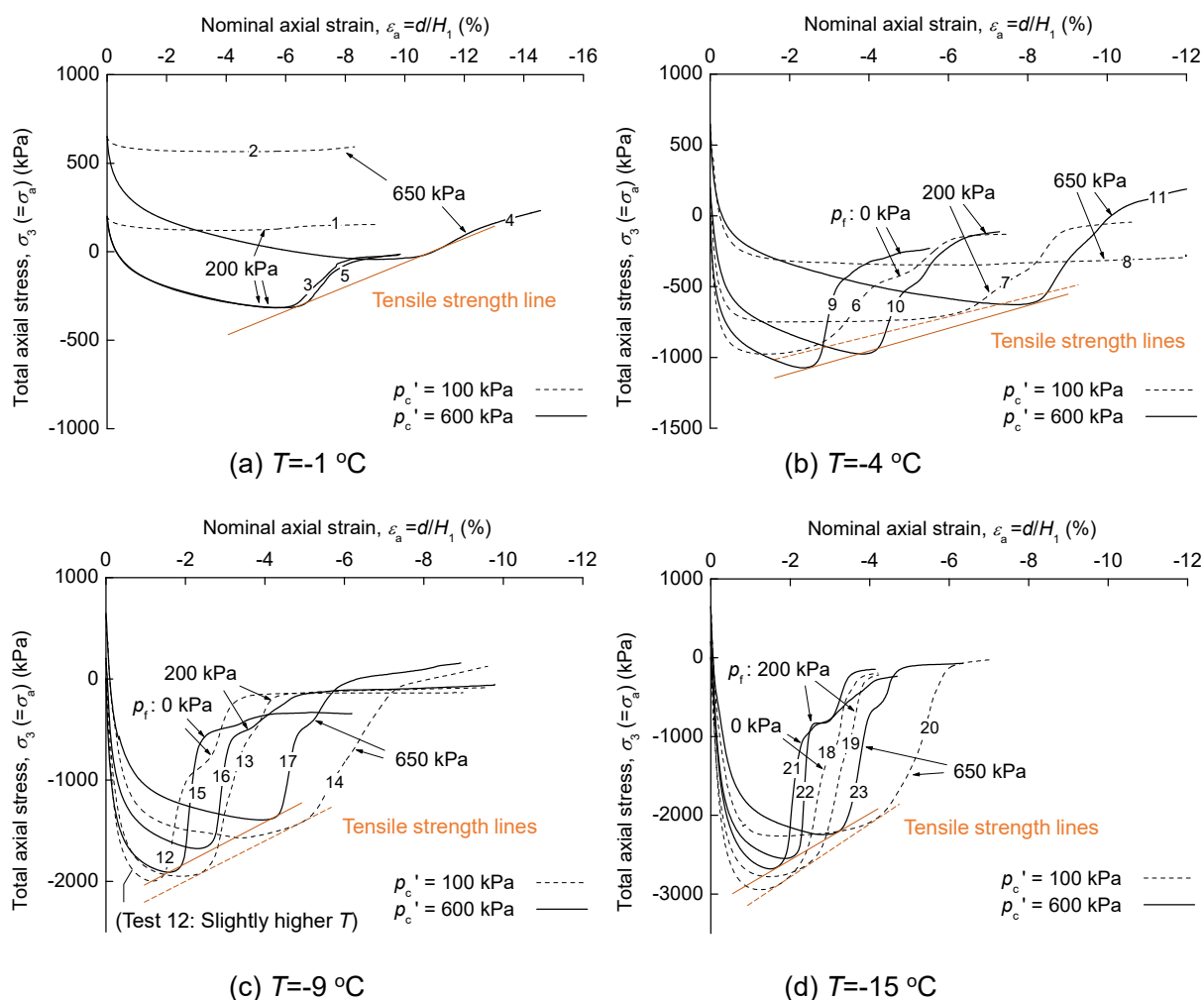
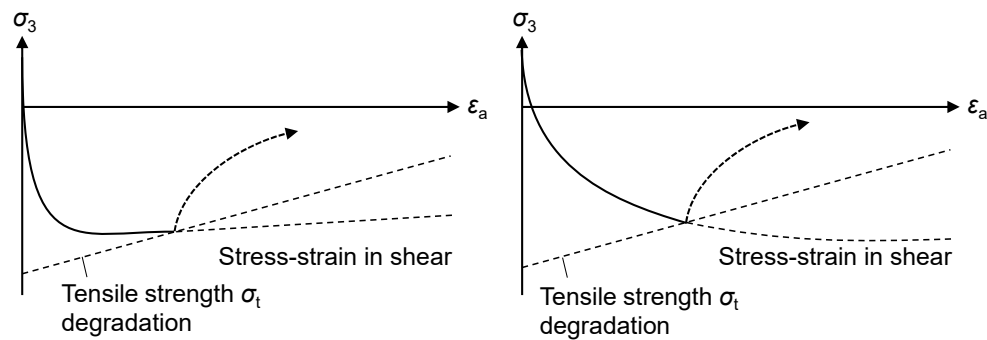


Figure 10: Axial stress – axial strain relationships from Tests 1-23
(The numbers indicate test ID)

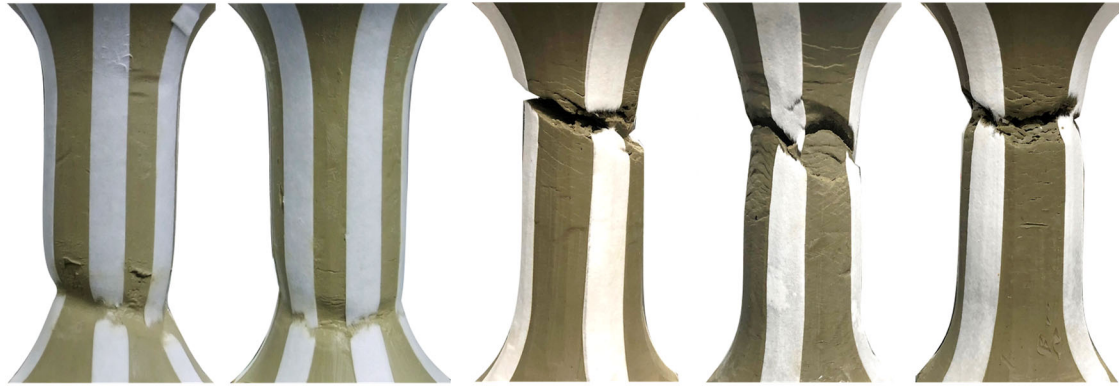
Another perspective offers a clearer view of the possible process of failure. **Figure 10** replots **Figure 8** in terms of axial stress $\sigma_a = \sigma_3$. For each p_f and T condition, the failure points are neatly aligned along a single line. A possible mechanism hypothesised from this observation is that the tensile strength is not constant but decreases as the shear strain accumulates. If the stress-strain relationship shows comparatively higher initial stiffness and smaller strain to peak shear resistance, the peak q value is dictated by the shear resistance, and only the post-peak behaviour is affected by tensile failure, as illustrated in **Figure 11(a)**. This was the case for $T = -4$ and -15 °C, $p_c' = 100$ kPa. In the other cases, the intersection of the decreasing tensile strength line with the stress-strain curve occurred before the latter reached the peak, as shown in **Figure 11(b)**. In such cases, lower p_f (and hence lower σ_3 for a given q since $\sigma_3 = p_f + q$) leads to higher q (lower $|q|$) as it meets the tensile strength line earlier.



(a) Smaller p_c' and larger ice content:
Smaller shear strength and larger initial
stiffness

(b) Larger p_c' and smaller ice content:
Larger shear strength and smaller initial
stiffness

Figure 11: Schematic illustration of shear hardening and tensile strength degradation
simultaneously at work



Test 1

Test 2

Test 3

Test 4

Test 5

(a) $T = -1\text{ }^{\circ}\text{C}$



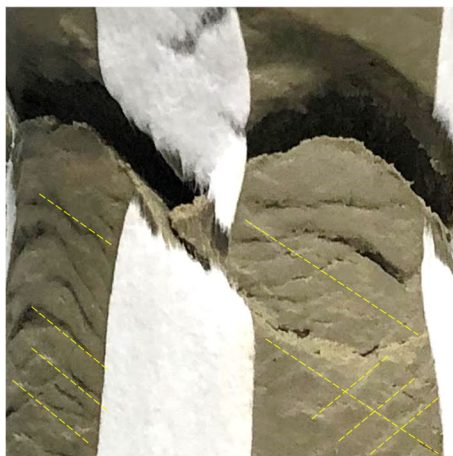
Test 8

Test 21

(Similar in all the rest)

(b) $T = -4, -9\text{ and }-15\text{ }^{\circ}\text{C}$

Figure 12: Failure modes of specimens in extension



(a) Test 4: Conjugate shear surfaces

(b) Test 22: Typical rupture surface

Figure 13: Close-up of failure

Almost all the tests exhibited a clear tensile failure surface at the end, as shown in **Figure 12(b)**, right) and **Figure 13(b)**. The surface was perpendicular to the axis, and the surface texture was rough with no trace of shear. The exceptions include Test 8, which did not reach clear failure despite significant extension beyond -12%. The other exceptions are Test 1-5, performed at $T=-1\text{ }^{\circ}\text{C}$ (more accurately, around $-0.7\text{ }^{\circ}\text{C}$). These tests exhibited only marginally higher strength than unfrozen states, due to the significant unfrozen water content. It is probably also relevant that the sample had been frozen initially to $-20\text{ }^{\circ}\text{C}$ and thawed back to $-0.7\text{ }^{\circ}\text{C}$. This freezing and undrained 'half-thawing' might have led to significant softening by generating excess pore water pressure (Nishimura et al., 2020). As a result, the strength was very low, and σ_3 remained positive at failure in Tests 1 and 2. The failure in these tests was therefore triaxial extension shear without involving eventual tensile failure, as shown in **Figure 12(a)**. In the tests with $p_c'=600\text{ kPa}$ (Tests 3-5), σ_3 did decrease to negative values (i.e. tensile stress). While these tests eventually showed tensile failure in form of rupture, diagonal traces of triaxial extension shear had developed as seen in **Figure 12(a)** due to the large shear strain before reaching the tensile failure line; $\epsilon_a=-6.2\%$, -10.8% and -6.5% in Tests 3, 4 and 5, respectively. A close-up view of the shear traces is shown in **Figure 13(a)**. Conjugate shear surfaces with approximately 30° dip were formed, along which the tensile rupture occurred, unlike at lower temperatures where the tensile rupture was almost horizontal. These tests almost failed in triaxial extension shear, only engaging the decreasing tensile strength after shear localisation occurred.

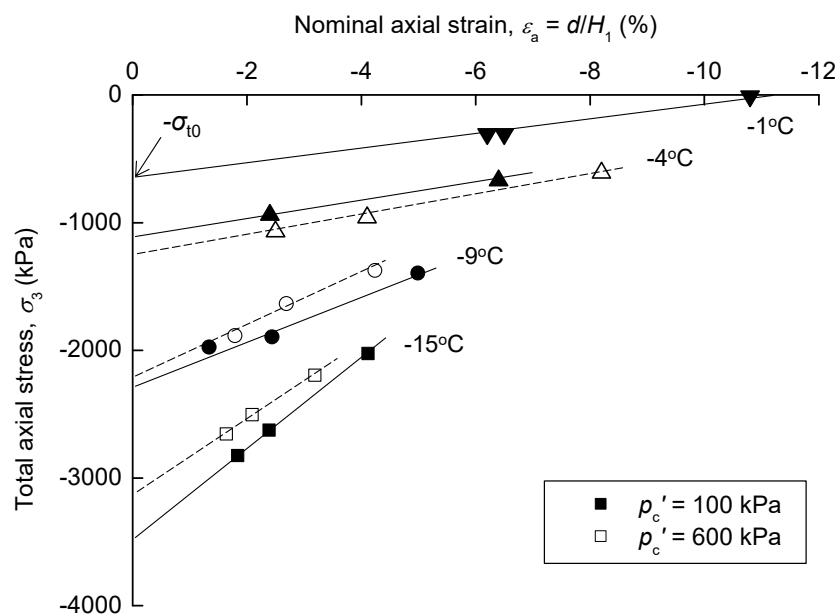
Initial tensile strength and degradation

The above observations suggest that the rather ambiguous nature of the failure envelopes in **Figure 9** – neither completely flat nor obviously stress-dependent – can be explained by a fine balance of two competing factors; the rate of strain-hardening in shear deformation, and the rate of tensile strength degradation, as illustrated in **Figure 11**. In general, smaller p_c' led to faster initial strain-hardening. For same Kasaoka clay, Wang et al. (2017; 2019) found that the initial stiffness was higher for lower p_c' due to larger w and hence larger ice content, while the peak shear strength was lower for lower p_c' due to less inter-soil particle friction. The pre-peak strain in shear therefore tended to be smaller for lower p_c' , as seen in **Figure 8**. Mobilising the shear strength, which was not post-freezing stress-dependent, before engaging the tensile strength led to generally flatter peak strength envelope for $p_c'=100\text{ kPa}$.

One of the key issues in understanding the limit strength is the tensile strength degradation during shear. **Figure 14(a)** summarises the tensile strength lines taken from **Figure 10** for all the conditions. Although there is a consistent trend, different slopes make the description difficult. When the same envelopes are replotted against the specific shear work input (i.e. the area between the $q - \epsilon_a$ curve and $q=0$ line in **Figure 10**), the relationships have an almost constant slope, as shown in **Figure 14(b)**. This slope can be used for tensile strength degradation modelling. The intercept

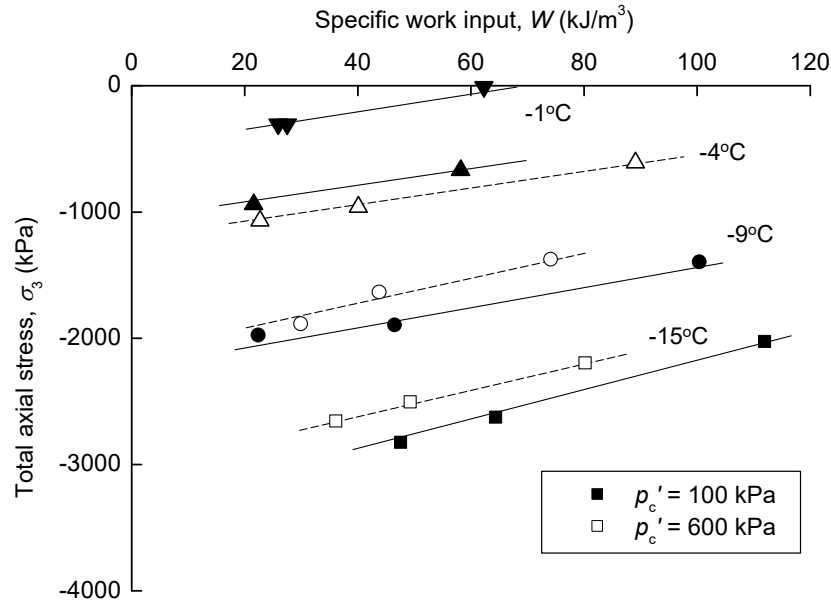
at $\varepsilon_a=0$ is the initial tensile strength σ_{t0} , or a hypothetical tensile strength that would be observed if the shear stress-strain relationship were perfectly rigid plastic. The σ_{t0} values are plotted against temperature T in **Figure 15**, along with the actually observed maximum $|q|$ ($=|q|_{\max}$) in the triaxial tensile Tests 1-2, 6-8, 14, 18-20. These tests are likely to have mobilised the shear strength before reaching the tensile failure. Also shown are $|q|_{\max}$ values from triaxial compression tests (Wang et al., 2017), corrected for the strain rate difference. Although the anisotropy and the intermediate principal stress (σ_2)-effect lead to different trends, these $|q|_{\max}$ values represent the shear strength. They are seen to be only slightly lower than σ_{t0} . Therefore, whether the limit strength in extension is determined by reaching the potential maximum shear strength or being cut short by degrading tensile strength (i.e. shear-induced reduction from σ_{t0}) depends on the fine balance of these mechanisms.

Interestingly, σ_{t0} is higher than the ice tensile strength compiled by Cuda and Ash (1984), despite the strain rate slower by one order (0.05%/min against 0.9%/min) and significant unfrozen water content in the clay. The microscopic failure of ice in the clay's small pores is probably harder to develop, just as the pore liquid water is harder to cavitate.



(a) Degradation against (nominal) axial strain

(Figure 14: Continues to next page)



(b) Degradation against specific work input

Figure 14: Summary of all the tensile strength lines and the strength degradation due to shear

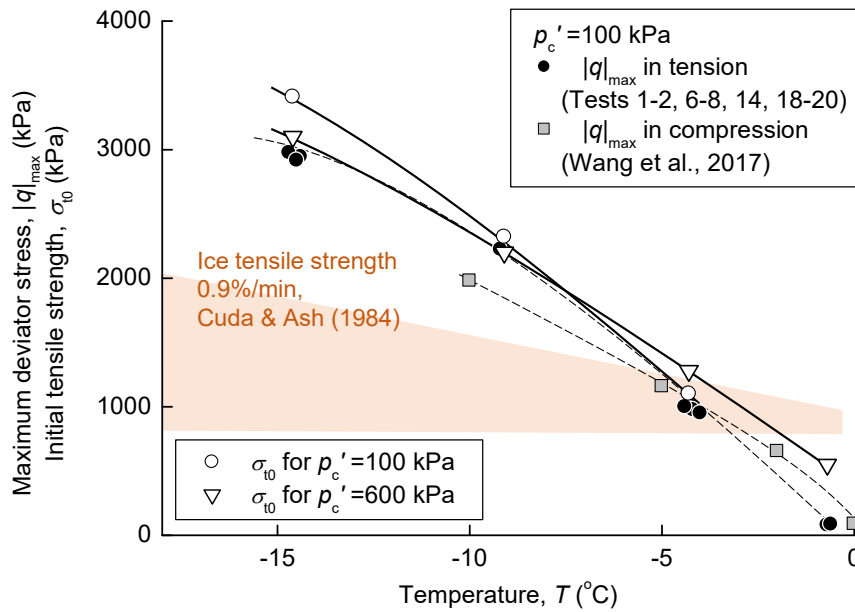


Figure 15: Initial tensile strength against temperature, in comparison with shear strength

TENSILE STRENGTH FOR MORE GENERAL STATES

Pore water pressure effects: Tests 24-26

Test 24-26 applied a higher pre-freezing back pressure u_c of 550 kPa, while the samples were consolidated at $p'_c = 100$ kPa. **Figure 16** compares these tests with Tests 18-20, with same $p'_c = 100$

kPa and $T=-15\text{ }^{\circ}\text{C}$ but with $u_c=100\text{ kPa}$. The higher back pressure only marginally affected the failure, providing a small extra strain before the tensile rupture at each p_r . The multi-phase coupled system theory by Nishimura and Wang (2019) does not differentiate these cases for shear behaviour, as a frozen state is essentially an undrained state, and the pore water (ice + liquid) pressure at frozen state will be only dependent on the initial effective stress, just as in the unfrozen soil mechanics. In Test 24, for example, the pore water pressure would decrease by 450 kPa in this theory when eventually p_r was reduced from 650 kPa to 200 kPa, bringing it to the same level as in Test 19. The almost same results seen for Tests 18-20 and 24-26 confirm the theory. A possible explanation for the slight difference is that less air escapes from the pore water when it turns ice under higher pressure, giving the pore ice with less defect. **Figure 16** suggests, however, that this effect is negligible in practice.

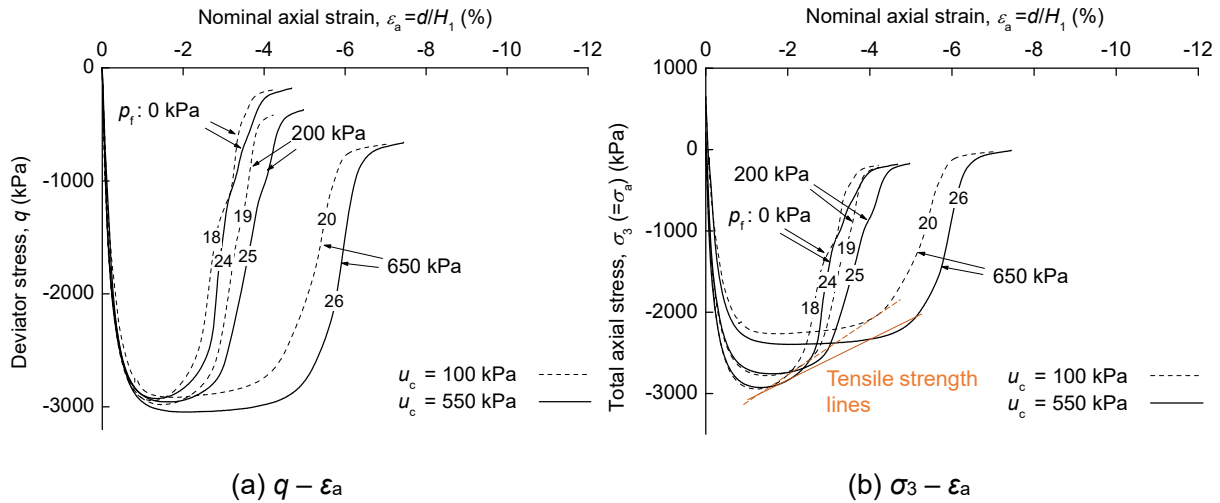


Figure 16: Influence of initial (pre-freezing) back pressure on stress-strain curves at $-15\text{ }^{\circ}\text{C}$

Major principal stress σ_1 changes: Test 30

The framework of shear-induced degradation of the tensile strength was tested for more general testing conditions. Test 30 involved reduction of the radial stress σ_r (= the major principal stress σ_1) from 650 kPa to 0 kPa after reaching $\epsilon_a=-6\%$, or 75% of ϵ_a at tensile rupture. When the extension was resumed with $\sigma_1=0\text{ kPa}$, the $q - \epsilon_a$ curve obviously overshoot the tensile strength line established from Tests 9-11 with same $T=-4\text{ }^{\circ}\text{C}$ and $p_c'=600\text{ kPa}$, as shown in **Figure 17(a)**. However, a closer look at the σ_1 -reduction stage in **Figure 17(b)** reveals that the failure actually had initiated at Point b. As the axial ram was fixed, the σ_3 change is a spontaneous reaction to σ_1 reduction. It usually changes parallelly with σ_1 to keep q constant (because there is no shear strain change), but at Point b, there was a temporary rebound of σ_3 to Point c. These points fall exactly on the expected tensile strength line. The fact that the test reached tensile failure immediately after the overshooting

to point d suggests the strength is still bound by this line, despite the temporary excessive strength. This overshoot is similar to TESRA behaviour proposed by Tatsuoka et al. (2002), reflecting the temporary effect of strain acceleration due to sudden loading restart.

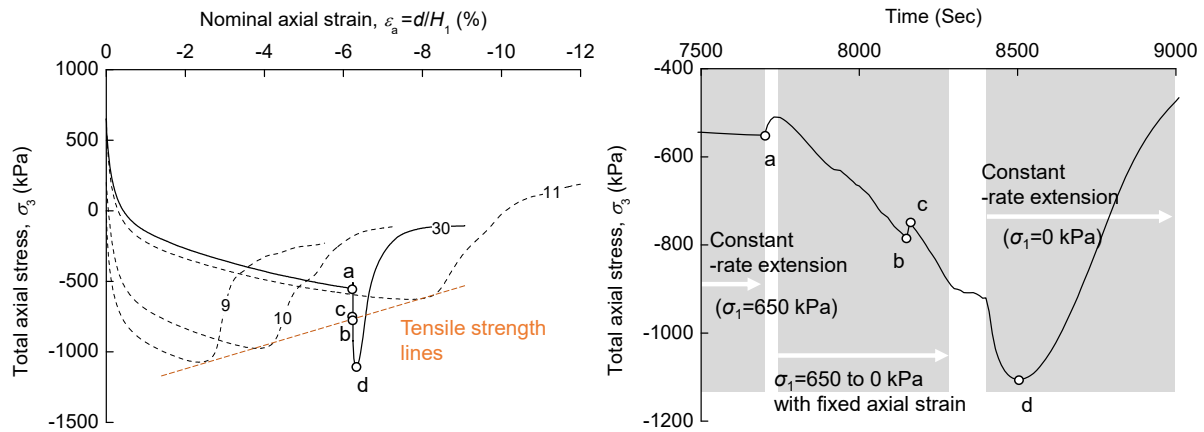


Figure 17: Effect of σ_1 reduction: Stress-strain relationship in Test 30

Time to failure and temperature changes: Tests 27-29

A temperature change from $T = -4$ °C to -15 °C was conducted during extension in Test 27. As described earlier, a pause of 4 hours was set between the unloading and reloading to allow temperature equilibrium at the specimen core. Reloading after cooling to -15 °C resulted in considerably high tensile stress, as shown in **Figure 18**, unbound by the established tensile strength line. The peak q , observed at around -3000 kPa, is the value expected if Test 23 could continue shear deformation without being bound by the tensile strength line. Obviously, 4-hour cooling 'healed' the tensile strength degradation induced by the previous shear up to $\epsilon_a = -6\%$. It was not clear, however, whether the cooling or the pause was responsible for this. Tests 28 and 29 were therefore conducted, in which similar unloading, 4-hour pause and reloading was conducted but without T change. **Figure 18** shows that the pause alone has limited healing effect, only moderately affecting the tensile strength line. The observed full recovery of the tensile strength by cooling cannot be explained just by the additional freezing of unfrozen pore water, because **Figure 5** suggests S_i reduction of only 10% from -4 °C to -15 °C. Regelation of the damaged ice must have also occurred. A longer pause, or more generally, a longer time to failure including slower loading rates, may have greater influence on the tensile strength line. The different loading rate conditions affect the shear stress-strain curves too. Obviously more study is necessary in incorporating the combined effects of temperature and deformation rate into the tensile strength framework.

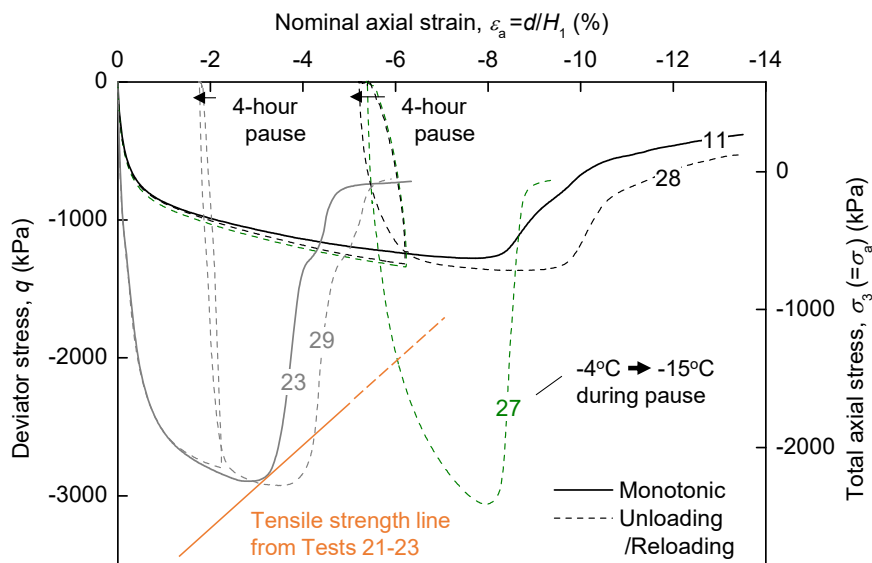


Figure 18: Influence of pause and/or temperature decrease (Tests 27-29) on stress-strain relationship: Comparison at $p_c'=600$ kPa and $p_f=650$ kPa

CONCLUSIONS AND IMPLICATIONS

A series of 'triaxial tension' tests was conducted on frozen Kasaoka clay, in which the axial stress was reduced to negative values while zero or positive radial stress was maintained. The samples were consolidated to different stresses in the triaxial cell and frozen without releasing the pressure before the tension tests, as expected in artificial ground freezing. This testing method enabled investigating the influence of the pre-freezing consolidation effective stress, post-freezing total radial stresses as well as the initial pore water pressure – a feature not attained in the conventional uniaxial tensile, split or bending tests.

Apparently flat to sub-flat failure envelopes, showing undecisive influence of stress, to Mohr's stress circle were obtained. It was shown, however, that they are explicable by considering two competing mechanisms; shear strain-hardening and tensile strength degradation. The former is independent of the confining (or radial) stress in Kasaoka clay for the studied stress range (0-650 kPa), while the latter is uniquely correlated to the specific work input as shear deformation progresses. A peak shear strength may be mobilised before tension rupture eventually occurs, or the tensile loading may be cut short by engaging the degrading tensile strength before attaining the peak shear strength. Question (i) raised in the introduction has been thus answered – both tensile and shear strengths play a role.

The tensile strength is described by two factors; the initial tensile strength, or a hypothetical strength

601 mobilised at zero shear strain, and its degradation rate as the soil structure is disturbed by shearing.
602 They are strongly dependent on the temperature, although the degradation rate can be normalised
603 by using the specific work input. More modest influence comes from the initial pore water pressure
604 and time to failure. The higher the pore water pressure, and the longer the time to failure, the frozen
605 clay endured to slight larger strains before eventually failing in tensile rupture. An interesting
606 phenomenon was observed that cooling from -4 °C to -15 °C just before the tensile failure
607 apparently healed the damage and fully recovered the tensile strength even at large strain.
608 Elucidating more generally the combined effect of temperature changes and loading rate (or time
609 to failure) requires much further investigation. These observations answer questions (ii) and (iv),
610 while leaving a room for further research.

611
612 In a more practical perspective, it may be acceptable to approximate the clay's failure envelope,
613 such as shown in **Figure 9**, as flat and stress-independent, except at very warm, half-thawing
614 temperatures (above -1 °C, for example). It should be remembered, however, that such envelopes
615 do not reflect the deformability after reaching the limit tensile stress. Given the abrupt loss of
616 resistance in tensile failure, a safety margin in design should take account of the deformability. The
617 ductile behaviour such as observed in Test 8 (-4 °C) in **Figure 8** is assuring when exploiting the
618 tensile strength in design, while colder temperatures lead to much more brittle behaviour. The
619 proposed framework involving the work-induced tensile strength degradation model will be useful
620 in estimating not just the peak strength, but also the strain to reach it. This is a tentative answer to
621 question (iii).

622 623 ACKNOWLEDGMENTS

624 This study was conducted with JSPS Kakenhi Grant-in-Aid 22H01582. The authors are grateful for
625 the funding.

626 627 REFERENCES

- 628 Akagawa, S. (2021) Artificially frozen ground and related engineering technology in Japan.
629 Sciences in Cold and Arid Regions 13 (2) 77-86. DOI: 10.3724/SP.J.1226.2021.20046.
- 630 Akagawa, S. and Nishisato, K. (2009) Tensile strength of frozen soil in the temperature range of
631 the frozen fringe. Cold Regions Science and Technology 57 13-22. DOI:
632 10.1016/j.coldregions.2009.01.002
- 633 Azmatch, T. F., Sego, D. C., Arenson, L. U. and Biggar, K. W. (2011) Tensile strength and stress-
634 strain behaviour of Devon silt under frozen fringe conditions. Cold Regions Science and
635 Technology 68 85-90. DOI: 10.1016/j.coldregions.2011.05.002
- 636 Bragg, R. A. and Andersland, O. B. (1981) Strain rate, temperature, and sample size effects on
637 compression and tensile properties of frozen sand. Engineering Geology 18 (1) 35-46. DOI:
638 10.1016/0013-7952(81)90044-2

639 Chamberlain, E., Groves, C. and Perham, R. (1972) The mechanical behaviour of frozen earth
640 materials under high pressure triaxial test conditions. *Géotechnique* 22 (3) 469–483. DOI:
641 10.1680/geot.1972.22.3.469

642 Cuda, V. Jr. and Ash, R. L. (1984) Development of a uniaxial ice tensile specimen for low
643 temperature testing. *Cold Regions Science and Technology* 9 47-52. DOI: 10.1016/0165-
644 232X(84)90047-8

645 Eckardt, H. (1982) Creep tests with frozen soils under uniaxial tension and uniaxial compression.
646 The Proceedings of the 4th Canadian Permafrost Conference, Calgary, Alberta, Eds. French, H.
647 M., National Research Council of Canada, Ottawa, Canada 394-405.

648 Haynes, D. and Karalius, J. A. (1977) Effect of temperature on the strength of frozen silt. CRREL
649 Report 77-3 27p.

650 Jessberger, H. L. (1981) A state-of-the-art report. Ground freezing: Mechanical properties,
651 processes and design. *Engineering Geology* 18 (1) 5-30. DOI: 10.1016/B978-0-444-42010-
652 7.50006-2

653 Ladanyi, B. and Morel, J.-F. (1990) Effect of internal confinement on compression strength of frozen
654 sand. *Canadian Geotechnical Journal* 27 (1) 8–18. DOI: 10.1139/t90-002

655 Li, Y., Ling, X., Su, L., An, L., Li, P. and Zhao, Y. (2018) Tensile strength of fiber reinforced soil under
656 freeze-thaw condition. *Cold Regions Science and Technology* 146 53-59. DOI:
657 10.1016/j.coldregions.2017.11.010

658 Namikawa, T. and Koseki, J. (2007) Evaluation of tensile strength of cement-treated sand based
659 on several types of laboratory tests. *Soils and Foundations* 47 (4) 657-674. DOI:
660 10.3208/sandf.47.657

661 Nishimura, S. and Wang, J. (2019) A simple framework for describing strength of saturated frozen
662 soils as multi-phase coupled system. *Géotechnique* 69 (8) 659-671 DOI: 10.1680/jgeot.17.P.104

663 Nishimura, S., Okajima, S., Joshi, B. R., Higo, Y. and Tokoro, T. (2020) Volumetric behaviour of
664 clays under freeze-thaw cycles. *Géotechnique* 71 (12) 1150-1164. DOI: 10.1680/jgeot.20.P.047

665 Ou, C.-Y., Kao, C.-C. and Chen, C.-I. (2009) Performance and analysis of artificial ground freezing
666 in the shield tunneling. *Journal of GeoEngineering* 4 (1) 29-40. DOI: DOI:
667 10.6310/jog.2009.4(1).4

668 Parameswaran, V. R. (1980) Deformation behaviour and strength of frozen sand. *Canadian*
669 *Geotechnical Journal* 17 (1) 74-88. DOI: 10.1139/t80-007

670 Rist, M. A. and Murrell, S. A. F. (1994) Ice triaxial deformation and fracture. *Journal of Glaciology*
671 40 (135) 305-318. DOI: 10.3189/S00222143000007395

672 Shulson, E. M. (2001) Brittle failure of ice. *Engineering Fracture Mechanics* 68 1839-1887. DOI:
673 10.1016/S0013-7944(01)00037-6

674 Singh, S. K. and Jordaan, I. J. (1996) Triaxial tests on crushed ice. *Cold Regions Science and*
675 *Technology* 24 153-165. DOI: 10.1016/0165-232X(95)00017-6

676 Tamrakar, S. B., Mitachi, T. and Toyosawa, Y. (2007) Measurement of soil tensile strength and

677 factors affecting its measurements. *Soils and Foundations* 47 (5) 911-918. DOI:
678 10.3208/sandf.47.911

679 Tatsuoka, F., Ishihara, M., di Benedetto, H. and Kuwano, R. (2002) Time-dependent shear
680 deformation characteristics of geomaterials and their simulation. *Soils and Foundations* 42 (2)
681 103-129. DOI: 10.3208/sandf.42.2_103

682 Tsuji, R. and Yoshida, T. (2019) Rational design of the artificial ground freezing with state-of-the-art
683 techniques. *Proceedings of the 16th Asian Regional Conference on Soil Mechanics and*
684 *Geotechnical Engineering, Taipei, Paper No. SA10-01-007.*

685 Uchida, K., Shioi, Y., Hirukawa, T. and Tatsuoka, F. (1993) The Trans-Tokyo Bay Highway Project
686 – A huge project currently under construction. *The Proceedings of Transportation Facilities*
687 *through Difficult Terrain, Snowmass, Colorado, USA, Eds. Wu, J. T. H. & Barrett, R. K., Balkema,*
688 *Rotterdam, The Netherlands* 57-87.

689 Viggiani, G. M. B., Casini, F., Winter, M. G., Smith, D. M., Eldred, P. J. L. and Toll, D. G. (2015)
690 Artificial ground freezing: from applications and case studies to fundamental research.
691 *Proceedings of the 16th ECSMGE Geotechnical Engineering for Infrastructure and Development,*
692 *ICE Publishing* 65–92. DOI:10.1680/ecsmge.60678

693 Wang, D., Ma, W. and Chang, X. (2004) Analyses of behavior of stress-strain of frozen Lanzhou
694 loess subjected to K_0 consolidation. *Cold Regions Science and Technology* 40 (1) 19-29. DOI:
695 10.1016/j.coldregions.2004.03.002

696 Wang, J., Nishimura, S. and Tokoro, T. (2017) Laboratory study and interpretation of mechanical
697 behavior of frozen clay through state concept. *Soils and Foundations* 57 (2) 194-210. DOI:
698 10.1016/j.sandf.2017.03.003

699 Wang, J., Nishimura, S., Joshi, B. R. and Okajima, S. (2019) Small-strain deformation
700 characteristics of frozen clay from static testing. *Géotechnique* 69 (9) 816-827. DOI:
701 10.1680/jgeot.18.P.115

702 Yamamoto, Y. and Springman, S. M. (2017) Three- and four-point bending tests on artificial frozen
703 soil samples at temperature close to 0 °C. *Cold Regions Science and Technology* 134 20-32.
704 DOI: 10.1016/j.coldregions.2016.11.003

705 You, Z., Ma, Y., Wang, Z. and Ma, J. (2021) Tensile strength variation of a silty clay under different
706 temperature and moisture conditions. *Cold Regions Science and Technology* 189 103314. DOI:
707 10.1016/j.coldregions.2021.103314

708 Zhang, J., Fu, H., Huang, Z., Wu, Y., Chen, W. and Shi, Y. (2019) Experimental study on the tensile
709 strength and failure characteristics of transversely isotropic rocks after freeze-thaw cycles. *Cold*
710 *Regions Science and Technology* 163 68-77. DOI: 10.1016/j.coldregions.2019.04.006

711 Zhou, G., Hu, K., Zhao, X., Wang, J., Liang, H. and Lu, G. (2015) Laboratory investigation on tensile
712 strength characteristics of warm frozen soils. *Cold Regions Science and Technology* 113 81-90.
713 DOI: 10.1016/j.coldregions.2015.02.003

714 Zhu, Y. and Carbee, D. L. (1985) Strain rate effect on the tensile strength of frozen silt. *The*

715 Proceedings of the 4th International Symposium on Ground Freezing, Sapporo, Japan, Eds.
716 Kinoshita, S. and Fukuda, M., Balkema, Rotterdam, The Netherlands 153-157.
717 Zhu, Y. and Carbee, D. L. (1987) Tensile strength of frozen silt. CRREL Report 87-15. 23p.

718

719

720 LIST OF NOTATIONS

721 A_2 : Area of the middle part of the specimen

722 D_1, D_2 : Diameters of the end and middle parts of the specimen

723 e_c : Void ratio after consolidation

724 H_1, H_2 : Total and middle part heights of the specimen

725 p_c' : The effective mean effective stress at consolidation

726 p_r : The total mean effective stress after freezing and before extension

727 $q, |q|_{\max}$: Deviator stress (=axial stress – radial stress) and its absolute maximum value

728 S_i : Degree of liquid saturation (=volume of ice / volume of pore)

729 s_u : Undrained shear strength

730 T : Temperature

731 u : Pore water pressure

732 u_0 : Back pressure

733 u_c : Pore water pressure after consolidation (= back pressure in the experiment)

734 u_{\min} : The minimum sustainable pore water pressure

735 w : Water content

736 w_u : Gravimetric unfrozen water content

737 $\varepsilon_1, \varepsilon_3$: Major and minor principal strains

738 $\varepsilon_a, \varepsilon_r$: Axial and radial strains (= ε_3 and ε_1 , respectively)

739 σ, σ' : Generic expressions for total and effective normal stresses

740 $\sigma_1, \sigma_2, \sigma_3$: Major, intermediate, and minor principal stresses

741 $\sigma_{1f}, \sigma_{3f}, \sigma_{1f}', \sigma_{3f}'$: Major and minor principal stresses at failure, and their effective values

742 σ_a, σ_r : Axial and radial stresses (= σ_3 and σ_1 , respectively)

743 σ_t, σ_t' : Total and effective tensile strength

744 σ_{t0} : (Total) tensile strength at zero shear strain

745 σ_{vp}' : One-dimensional pre-consolidation effective stress

746 τ : Shear stress